

# Thermal Decomposition Reaction and a Comprehensive Kinetic Model of Dimethyl Ether

ZHENWEI ZHAO, MARCOS CHAOS, ANDREI KAZAKOV, FREDERICK L. DRYER

Department of Mechanical and Aerospace Engineering, Princeton University, Princeton, NJ 08544

Received 1 August 2006; revised 18 May 2007, 24 July 2007; accepted 27 July 2007

DOI 10.1002/kin.20285

Published online in Wiley InterScience (www.interscience.wiley.com).

**ABSTRACT:** The unimolecular decomposition reaction of dimethyl ether (DME) was studied theoretically using RRKM/master equation calculations. The calculated decomposition rate is significantly different from that utilized in prior work (Fischer et al., *Int J Chem Kinet* 2000, 32, 713–740; Curran et al., *Int J Chem Kinet* 2000, 32, 741–759). DME pyrolysis experiments were performed at 980 K in a variable-pressure flow reactor at a pressure of 10 atm, a considerably higher pressure than previous validation data. Both unimolecular decomposition and radical abstraction are significant in describing DME pyrolysis, and hierarchical methodology was applied to produce a comprehensive high-temperature model for pyrolysis and oxidation that includes the new decomposition parameters and more recent small molecule/radical kinetic and thermochemical data. The high-temperature model shows improved agreement against the new pyrolysis data and the wide range of high-temperature oxidation data modeled in prior work, as well as new low-pressure burner-stabilized species profiles (Cool et al., *Proc Combust Inst* 2007, 31, 285–294) and laminar flame data for DME/methane mixtures (Chen et al., *Proc Combust Inst* 2007, 31, 1215–1222). The high-temperature model was combined with low-temperature oxidation chemistry (adopted from Fischer et al., *Int J Chem Kinet* 2000, 32, 713–740), with some modifications to several important reactions. The revised construct shows good agreement against high- as well as low-temperature flow reactor and jet-stirred reactor data, shock tube ignition delays, and laminar flame species as well as flame speed measurements. © 2007 Wiley Periodicals, Inc. *Int J Chem Kinet* 40: 1–18, 2008

Correspondence to: Frederick L. Dryer; e-mail: fldryer@princeton.edu.

Present address of Andrei Kazakov: National Institute of Standards and Technology, Thermodynamics Research Center, Boulder, CO 80305.

Contract grant sponsor: Chemical Sciences, Geosciences, and Biosciences Division, Office of Basic Energy Sciences, Office of Science, U.S. Department of Energy.

Contract grant number: DE-FG02-86ER13503.

Additional chemical kinetic data are available as Supplementary Material at <http://www.interscience.wiley.com/jpages/0538-8066/suppmat/>.

© 2007 Wiley Periodicals, Inc.

## INTRODUCTION

As a result of its high-cetane number and low-sooting characteristics, dimethyl ether (DME) has been proposed as a promising alternative diesel fuel and fuel additive for reducing particulate and NO<sub>x</sub> emissions. Several experimental [1–11] and theoretical (e.g., [12–14]) studies have considered DME oxidation and pyrolysis characteristics previously. A detailed kinetic mechanism for DME oxidation and pyrolysis [1,2]

and its updated version [3] was developed based in part on comparisons with data from the Princeton Variable-Pressure Flow Reactor (VPFR) over temperature and pressure ranges of 550–850 K and 12–18 atm, respectively. The model was also compared against results from a jet-stirred reactor [4,5], a shock-tube [6], and a counterflow diffusion flame [7]. More recently, Kaiser et al. [8] and McIlroy et al. [9] successfully compared model predictions with species profiles measured in low and atmospheric pressure, premixed, burner-stabilized flames. However, the ability of the model to predict laminar flame speeds has been questioned [10,11]. Since the development of this DME model [1,2], significant advances in fundamentals (mechanistic issues, thermochemical and kinetic parameters) have occurred particularly for  $\text{H}_2/\text{O}_2$  and  $\text{C}_1\text{--C}_2$  kinetics, which are especially relevant to flame conditions.

Moreover, the DME molecular decomposition reaction is significant at flow reactor, shock tube, and laminar flame conditions. Since the decomposition and abstraction pathways are coupled during both pyrolysis and oxidation, an accurate description of the DME unimolecular decomposition process over a wide range of conditions is needed to further understand the contributions of the abstraction reactions in kinetic models describing high-temperature DME combustion. In the present work, the thermal decomposition of DME was studied theoretically and new DME pyrolysis measurements at high pressure and temperature were obtained in the Princeton VPFR. A model was assembled in a hierarchical manner, which incorporates new kinetic developments in fundamental small molecules (e.g.,  $\text{H}_2$ ,  $\text{CO}$ ), encompasses recent small molecule/radical kinetics and thermochemistry updates, and implements the low-temperature reaction subset from [1,2] to yield a comprehensive model for DME combustion.

The calculated decomposition rate is significantly different from that used in prior studies [1,2]; however, the revised pyrolysis model better predicts the present pyrolysis measurements and literature data. Here, we show that further revisions of the DME comprehensive model allow for reasonable predictions of all of the prior literature data on DME pyrolysis and oxidation as well as new low-pressure DME burner-stabilized species data, and flame properties of DME/methane mixtures.

## EXPERIMENTAL METHODS

The new dimethyl ether pyrolysis experiments reported herein were performed in the Princeton VPFR. Only a brief discussion of these experiments is given below

as there exist several other publications providing detailed information on the VPFR instrumentation and experimental methodology (e.g., see [1]).

Nitrogen carrier gas is heated by a pair of electrical resistance heaters and directed into a reactor duct. The carrier gas flows around a baffle plate into a gap serving as the entrance to a diffuser. In the present study, a certified standard gaseous mixture of DME and nitrogen (5% DME by volume) was used as fuel and delivered to the flow reactor by a calibrated mass flow controller (accurate to  $\pm 1\%$  of full scale). The fuel/nitrogen mixture flows through a central injector tube and is rapidly mixed with a much larger flow of carrier gas through the reactor tube. The reactor is surrounded by electrical resistance thermostated heaters, which maintain the reactor the wall temperatures within close proximity ( $< 50$  K) of gas temperatures. The fuel/carrier gas mixture exits a mixer–diffuser section into a constant area test section. Near the exit of the test section, a sampling probe is positioned on the reactor centerline to continuously extract and convectively quench a small percentage of the flow. At the same axial location, the local reaction gas temperature is measured with a type R thermocouple accurate to  $\pm 3$  K.

The extracted sample gas flows via heated Teflon lines to analytical equipment including a Fourier transform infrared spectrometer (FTIR), an electrochemical  $\text{O}_2$  analyzer, and a pair of nondispersive infrared analyzers for  $\text{CO}$  and  $\text{CO}_2$ . Other stable species of interest (e.g.,  $\text{CH}_4$ ,  $\text{H}_2\text{O}$ ) are measured continuously online using FTIR spectrometry. The measurement uncertainties for the data reported here are  $\text{CH}_3\text{OCH}_3 \pm 4\%$ ,  $\text{CH}_2\text{O} \pm 5\%$ ;  $\text{O}_2 \pm 2\%$ ;  $\text{CH}_4 \pm 2\%$ ,  $\text{CO} \pm 2\%$ ;  $\text{CO}_2 \pm 2\%$  of reading.

The distance between the point of fuel injection and the sampling position is varied by moving the fuel injector probe (with attached mixer/diffuser assembly) relative to the fixed sampling location. Mean axial velocity measurements along the centerline of the reactor are used to correlate distance with residence time. By this means, profiles of stable species versus reaction residence time can be determined experimentally. The uncertainty in the residence time is approximately 5%.

Two types of flow reactor experiments, species-time history and reactivity experiments, are compared with predictions in this paper. The methods utilized herein to compare flow reactor data with plug flow model predictions have been discussed extensively in previous publications; nonetheless, the subject remains puzzling to some readers. An extensive summary and detailed discussion of time shifting, initialization, and “absolute time” comparison methodologies are provided as Supplementary Material.

## DIMETHYL ETHER UNIMOLECULAR DECOMPOSITION

During DME pyrolysis, initiation proceeds via unimolecular decomposition:  $\text{CH}_3\text{OCH}_3 = \text{CH}_3 + \text{CH}_3\text{O}$  (R1), and the rate of this reaction is known to be significant in comparison to abstraction reactions with DME at flow reactor temperatures. Few estimates of this rate and its pressure falloff have appeared in the literature previously. Here, the decomposition of DME was further investigated theoretically based on the RRKM/master equation approach in a manner similar to that used by Li et al. [15]. Initially, all of the competitive decomposition channels were considered, but their rate constants were found to be much lower than  $k_1$ , only becoming competitive at very high temperatures (above 3000 K). As a result, only the dominant channel, that is, reaction (R1), was considered in further detail.

Equilibrium geometries of the reactants and products were optimized by the hybrid density functional B3LYP method [16–19] with the 6-31G(d) basis set. Vibrational frequencies, calculated using the same method, were scaled by a factor of 0.96, and energies were computed at G3B3 level of theory [20]. The Gaussian 98 package [21] was used for all the molecular orbital calculations. We also compared the energy barriers (including a zero-point energy, correction at 0 K) calculated by different theoretical methods, as well as available experimental results. We found all theoretical results to be in reasonable agreement. In particular, the energy barrier obtained in the present study matches very well the recent *ab initio* results of Nash and Francisco [12]. Similar to Li et al. [15], special consideration was given to the two hindered rotations around  $\text{CH}_3$ -internal rotors to evaluate the rotational potentials and to compute the density of states. Further details of these calculations (e.g., listings of vibrational frequencies and rotational constants) as well as the computed rates (discussed below) are provided as a supplemental file.

The rate constants for the DME unimolecular decomposition were computed using an in-house computer code [15]. The microscopic rate coefficient for the simple-fission reaction (R1) was evaluated using the prescribed high-pressure limit for this channel and the molecular properties of reaction products. The high-pressure limit rate constant was calculated from microscopic reversibility using a rate expression of  $2.75 \times 10^{13} \text{ cm}^3/\text{mol/s}$  for the reverse reaction, that is, the recombination of  $\text{CH}_3\text{O}$  and  $\text{CH}_3$ . We estimated the rate expression in the reverse direction as the recombination of two radical species, which has no associated activation energy and an *A*-factor normally

varying between  $1 \times 10^{13}$  and  $3 \times 10^{13}$ , based on data for similar reactions [22–24]. The molecular parameters (reaction barriers, moments of inertia, and vibrational frequencies) are required as input for the sum and density-of-states computations, followed by the microscopic rate constant  $k(E)$  calculation based on RRKM theory [25]. With the input information for the collision model, rate constants were calculated after solving the master equation [25]. The in-house computer program was specifically designed for computational efficiency (thus allowing extensive parametric studies without sacrificing accuracy). These features include arbitrary energy and temperature dependence of  $\langle \Delta E_{\text{down}} \rangle$  (see below), a more rigorous treatment of hindered rotations, and evaluation of microscopic rate coefficients for loose transition states from the prescribed high-pressure limit rate constant.

The energy increment was fixed at  $1 \text{ cm}^{-1}$  in all sum and density-of-states computations. The standard form of the exponential-down model was used for collision energy transfer. In the absence of reliable measurements in the falloff region that are normally used to calibrate the collision model, the model parameters had to be assigned *a priori*. Specifically, following recommendations of Knyazev and Slagle [26] based on their extensive comparisons of theoretical predictions with the large body of experimental data, and accounting for both temperature and energy dependencies of the main collision model parameter, the energy transfer per downward collision,  $\langle \Delta E_{\text{down}} \rangle$ , was calculated using the following expression:  $\langle \Delta E_{\text{down}} \rangle = ATE^{1/2}$ , where *T* is the temperature, *E* is the internal energy, and *A* is an adjustable constant taken as  $4.313 \times 10^{-3}$  and  $3.458 \times 10^{-3} \text{ cm}^{-1/2} \text{ K}^{-1}$  for  $\text{N}_2$  and Ar, respectively, in the present study. This calculation yields a value for  $\langle \Delta E_{\text{down}} \rangle$  of about 217 and  $174 \text{ cm}^{-1}$  for  $\text{N}_2$  and Ar at 298 K and the energy corresponding to the barrier of reaction (R1), which agree with the values determined experimentally for similar reactions by Knyazev and Tsang [27]. The collision frequency of DME with the bath gas was estimated from the Lennard–Jones parameters adopted from Kee et al. [28]. An energy grain size of  $10 \text{ cm}^{-1}$  was used in the master equation solutions, and the resulting relaxation matrix size was  $7410 \times 7410$ . This grain size provided numerically convergent results for all temperatures and pressures considered in this study.

The calculated rate constant of reaction (R1) over the temperature range of 650–1350 K at 1 atm is presented in Fig. 1. The rate constant agrees well with the experimental data of Batt et al. [29] by utilizing a  $\langle \Delta E_{\text{down}} \rangle$  of  $300 \text{ cm}^{-1}$  at 298 K for DME, which is consistent with the experimental work of Knyazev and Tsang [27] for similar species. The rate constant

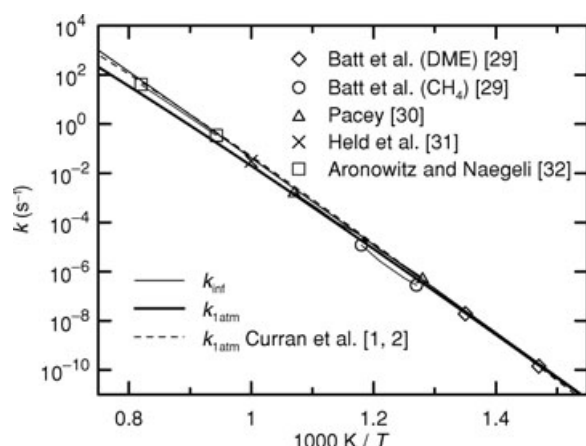


**Figure 1** Rate constant of the reaction  $\text{CH}_3\text{OCH}_3 = \text{CH}_3 + \text{CH}_3\text{O}$ .

at the high-pressure limit is in very good agreement with the measurement of Pacey [30]. However, the present theoretical work gives a value significantly lower than the experimental data reported by Held et al. [31] and Aronowitz and Naegeli [32]. To fit the data from [31,32], a rate constant of at least  $(1-2) \times 10^{14}$  has to be assigned to the reverse reaction of (R1), which is much higher than that of similar reactions obtained experimentally, for example [22–24], and theoretically [33]. High values of (R1) are also inconsistent with the empirical “geometric mean rule,” for example [34–36], which provides an estimate for the recombination rate coefficient of two radicals, A and B,  $k_{AB} = 2(k_{AA}k_{BB})^{1/2}$ , based on self-recombination rate coefficients  $k_{AA}$  and  $k_{BB}$  for A and B, respectively. By using experimental values for recombination of  $\text{CH}_3 + \text{CH}_3$  [37–39] and  $\text{CH}_3\text{O} + \text{CH}_3\text{O}$  [40], one obtains a rate coefficient of about  $2 \times 10^{13}$  for the reverse rate coefficient of R1, that is, a factor of 5–10 lower than the values needed to match the experimental data of [31,32].

The present rate coefficient at around 800 K is higher than the experimental data of Batt et al. [29] for the pyrolysis of DME in  $\text{CH}_4$  bath gas, by utilizing a  $\langle \Delta E_{\text{down}} \rangle$  of  $269 \text{ cm}^{-1}$  at 298 K (the value was recommended in [27]). By assigning either a rate constant of  $1.35 \times 10^{13}$  to the reverse reaction of (R1) or a  $\langle \Delta E_{\text{down}} \rangle$  of  $175 \text{ cm}^{-1}$  at 298 K, the calculated rate constant fits the data well. Even so, under all conditions, the present analysis results in a rate coefficient at 1 atm that is much lower (a factor of 3 at 1000 K) and exhibits a higher degree of falloff than that obtained by Curran et al. [2]. As a result of the relative importance of decomposition and radical abstractions from DME at flow reactor conditions, it is immediately

evident that the abstraction channel parameters present in the Curran et al. model are not compatible with the present decomposition parameters. Consequently, a revised model description was pursued.

## COMPREHENSIVE MODEL FOR DIMETHYL ETHER PYROLYSIS AND OXIDATION

The present dimethyl ether model was assembled in a hierarchical manner. The detailed chemical kinetic reaction mechanism consists of 290 reversible reactions amongst 55 species and is provided (along with associated thermodynamic and transport parameters) as a supplemental file. The high-temperature decomposition and oxidation portion of the model was updated to reflect recent advances in small molecule/radical kinetics and thermochemistry, to incorporate the new unimolecular decomposition results described above, and to re-evaluate both prior and new comparisons of predictions against DME pyrolysis and oxidation data. The present reaction scheme consists of a baseline  $\text{H}_2/\text{C}_1\text{-C}_2$  submodel recently developed in our laboratory for  $\text{H}_2$ [41],  $\text{H}_2/\text{CO}/\text{CH}_2\text{O}/\text{CH}_3\text{OH}$  [42], and  $\text{C}_2\text{H}_5\text{OH}$  [43,44]. Table I lists DME-related reactions that were considered along with the baseline models. The DME high-temperature subset contains reactions with  $\text{O}_2$  as well as the thermal decomposition (R1) as initiation steps. As the radical pool becomes established, H-atom abstraction from the fuel becomes more important. These propagation reactions involve radicals (e.g., H, O, OH,  $\text{HO}_2$ ,  $\text{CH}_3$ ,  $\text{CH}_3\text{O}$ ) reacting with the fuel. The methoxymethyl radical ( $\text{CH}_3\text{OCH}_2$ ) is formed by H-atom abstraction from DME. Its reactions include a thermal decomposition reaction forming formaldehyde and  $\text{CH}_3$  and reactions with  $\text{O}_2$ ,  $\text{HO}_2$ , O, OH,  $\text{CH}_3$ , and  $\text{CH}_3\text{O}$ .

Among the H-atom abstraction reactions, the reaction of fuel with the methyl radical ( $\text{CH}_3\text{OCH}_3 + \text{CH}_3 = \text{CH}_3\text{OCH}_2 + \text{CH}_4$  (R2)) is very important for describing fuel consumption at flow reactor and shock tube ignition delay conditions. The limited literature data for reaction (R2) are all restricted to low temperatures ( $\leq 1000 \text{ K}$ ). Rate measurements at higher temperatures are not well established and exhibit considerable uncertainty. For example, Pacey [30] reports activation energy values for reaction (R2) with an uncertainty of almost  $\pm 1.7 \text{ kcal/mol}$  with  $\log(A) = 10^{13.5 \pm 0.4}$ . During the course of this study, it was found necessary to increase the rate of reaction (R2) for temperatures higher than approximately 900 K. On the basis of these results, we performed least-squares modified Arrhenius fit of available experimental data [29–31,45] placing larger weight on the upper uncertainty estimates of Pacey

**Table I** Dimethyl Ether Reaction Submechanism; cm<sup>3</sup>/mol/sec/cal units

No.	Reaction	<i>A</i>	<i>n</i>	<i>E<sub>a</sub></i>	Reference
1	CH <sub>3</sub> OCH <sub>3</sub> = CH <sub>3</sub> + CH <sub>3</sub> O	(1 atm) 1.699E+42 (10 atm) 6.279E+35	-7.95 -5.89	9.181E+04 8.971E+04	* <sup>a</sup> * <sup>a</sup>
2	CH <sub>3</sub> OCH <sub>3</sub> + CH <sub>3</sub> = CH <sub>3</sub> OCH <sub>2</sub> + CH <sub>4</sub>	2.680E+01	3.78	9.631E+03	*
3	CH <sub>3</sub> OCH <sub>3</sub> + OH = CH <sub>3</sub> OCH <sub>2</sub> + H <sub>2</sub> O	6.710E+06	2.00	-6.299E+02	[48]
4	CH <sub>3</sub> OCH <sub>3</sub> + H = CH <sub>3</sub> OCH <sub>2</sub> + H <sub>2</sub>	2.970E+07	2.00	4.034E+03	[48]
5	CH <sub>3</sub> OCH <sub>3</sub> + O = CH <sub>3</sub> OCH <sub>2</sub> + OH	1.855E-03	5.29	-1.090E+02	†
6	CH <sub>3</sub> OCH <sub>3</sub> + HO <sub>2</sub> = CH <sub>3</sub> OCH <sub>2</sub> + H <sub>2</sub> O <sub>2</sub>	2.000E+13	0.00	1.650E+04	*
7	CH <sub>3</sub> OCH <sub>3</sub> + O <sub>2</sub> = CH <sub>3</sub> OCH <sub>2</sub> + HO <sub>2</sub>	4.100E+13	0.00	4.491E+04	†
8	CH <sub>3</sub> OCH <sub>3</sub> + CH <sub>3</sub> O = CH <sub>3</sub> OCH <sub>2</sub> + CH <sub>3</sub> OH	6.020E+11	0.00	4.074E+03	†
9	CH <sub>3</sub> OCH <sub>3</sub> + CH <sub>3</sub> OCH <sub>2</sub> O <sub>2</sub> = CH <sub>3</sub> OCH <sub>2</sub> + CH <sub>3</sub> OCH <sub>2</sub> O <sub>2</sub> H	5.000E+12	0.00	1.769E+04	†
10	CH <sub>3</sub> OCH <sub>2</sub> = CH <sub>2</sub> O + CH <sub>3</sub>	1.200E+13	0.00	2.575E+04	*
11	CH <sub>3</sub> OCH <sub>2</sub> + O <sub>2</sub> = CH <sub>3</sub> OCH <sub>2</sub> O <sub>2</sub>	2.000E+12	0.00	0.00	†
12	CH <sub>3</sub> OCH <sub>2</sub> O <sub>2</sub> + CH <sub>2</sub> O = CH <sub>3</sub> OCH <sub>2</sub> O <sub>2</sub> H + HCO	1.000E+12	0.00	0.00	†
13	CH <sub>3</sub> OCH <sub>2</sub> O <sub>2</sub> + CH <sub>3</sub> OCH <sub>2</sub> O <sub>2</sub> = O <sub>2</sub> + CH <sub>3</sub> OCH <sub>2</sub> O + CH <sub>3</sub> OCH <sub>2</sub> O	1.597E+23	-4.50	0.00	†
14	CH <sub>3</sub> OCH <sub>2</sub> O <sub>2</sub> + CH <sub>3</sub> OCH <sub>2</sub> O <sub>2</sub> = O <sub>2</sub> + CH <sub>3</sub> OCHO + CH <sub>3</sub> OCH <sub>2</sub> OH	6.844E+22	-4.50	0.00	†
15	CH <sub>3</sub> OCH <sub>2</sub> O <sub>2</sub> = CH <sub>2</sub> OCH <sub>2</sub> O <sub>2</sub> H	6.000E+10	0.00	2.150E+04	†
16	CH <sub>2</sub> OCH <sub>2</sub> O <sub>2</sub> H = CH <sub>3</sub> OCH <sub>2</sub> O + OH	2.106E+22	-2.12	4.383E+04	†
17	CH <sub>2</sub> OCH <sub>2</sub> O <sub>2</sub> H = OH + CH <sub>2</sub> O + CH <sub>2</sub> O	1.500E+13	0.00	2.050E+04	†
18	CH <sub>2</sub> OCH <sub>2</sub> O <sub>2</sub> H + O <sub>2</sub> = O <sub>2</sub> CH <sub>2</sub> OCH <sub>2</sub> O <sub>2</sub> H	7.000E+11	0.00	0.00	†
19	O <sub>2</sub> CH <sub>2</sub> OCH <sub>2</sub> O <sub>2</sub> H = HO <sub>2</sub> CH <sub>2</sub> OCHO + OH	4.000E+10	0.00	1.850E+04	†
20	HO <sub>2</sub> CH <sub>2</sub> OCHO = OCH <sub>2</sub> OCHO + OH	3.000E+16	0.00	4.000E+04	*
21	OCH <sub>2</sub> OCHO = HOCH <sub>2</sub> OCO	1.000E+11	0.00	1.400E+04	†
22	HOCH <sub>2</sub> OCO = HOCH <sub>2</sub> O + CO	2.177E+16	-2.69	1.720E+04	†
23	HOCH <sub>2</sub> OCO = CH <sub>2</sub> OH + CO <sub>2</sub>	5.311E+15	-2.61	2.081E+04	†
24	CH <sub>3</sub> OCH <sub>2</sub> + HO <sub>2</sub> = CH <sub>3</sub> OCH <sub>2</sub> O + OH	9.000E+12	0.00	0.00	†
25	CH <sub>3</sub> OCH <sub>2</sub> + CH <sub>2</sub> O = CH <sub>3</sub> OCH <sub>3</sub> + HCO	5.490E+03	2.80	5.862E+03	†
26	CH <sub>3</sub> OCH <sub>2</sub> + CH <sub>3</sub> O = CH <sub>3</sub> OCH <sub>3</sub> + CH <sub>2</sub> O	2.410E+13	0.00	0.00	†
Formic acid reactions					
27	HOCH <sub>2</sub> O = HCOOH + H	1.000E+14	0.00	1.490E+04	†
28	CH <sub>2</sub> O + OH = HOCH <sub>2</sub> O	4.500E+15	-1.11	0.00	†
29	HCOOH + M = CO + H <sub>2</sub> O + M	2.300E+13	0.00	5.000E+04	†
30	HCOOH + M = CO <sub>2</sub> + H <sub>2</sub> + M	1.500E+16	0.00	5.700E+04	†
31	HCOOH = HCO + OH	4.593E+18	-0.46	1.083E+05	†
32	HCOOH + OH = H <sub>2</sub> O + CO <sub>2</sub> + H	2.620E+06	2.06	9.160E+02	†
33	HCOOH + OH = H <sub>2</sub> O + CO + OH	1.850E+07	1.51	-9.620E+02	†
34	HCOOH + H = H <sub>2</sub> + CO <sub>2</sub> + H	4.240E+06	2.10	4.868E+03	†
35	HCOOH + H = H <sub>2</sub> + CO + OH	6.030E+13	-0.35	2.988E+03	†
36	HCOOH + CH <sub>3</sub> = CH <sub>4</sub> + CO + OH	3.900E-07	5.80	2.200E+03	†
37	HCOOH + HO <sub>2</sub> = H <sub>2</sub> O <sub>2</sub> + CO + OH	1.000E+12	0.00	1.192E+04	†
38	HCOOH + O = CO + OH + OH	1.770E+18	-1.90	2.975E+03	†
Methyl formate reactions					
39	CH <sub>3</sub> OCH <sub>2</sub> O = CH <sub>3</sub> OCHO + H	1.745E+16	-0.66	1.172E+04	†
40	CH <sub>3</sub> OCHO = CH <sub>3</sub> + OCHO	1.392E+18	-0.99	7.914E+04	†
41	OCHO + M = H + CO <sub>2</sub> + M	2.443E+15	-0.50	2.650E+04	†
42	CH <sub>3</sub> OCHO + O <sub>2</sub> = CH <sub>3</sub> OCO + HO <sub>2</sub>	1.000E+13	0.00	4.970E+04	†
43	CH <sub>3</sub> OCHO + OH = CH <sub>3</sub> OCO + H <sub>2</sub> O	2.340E+07	1.61	-3.500E+01	†
44	CH <sub>3</sub> OCHO + HO <sub>2</sub> = CH <sub>3</sub> OCO + H <sub>2</sub> O <sub>2</sub>	1.220E+12	0.00	1.700E+04	†
45	CH <sub>3</sub> OCH <sub>2</sub> O + O <sub>2</sub> = CH <sub>3</sub> OCHO + HO <sub>2</sub>	5.000E+10	0.00	5.000E+02	†
46	CH <sub>3</sub> OCH <sub>2</sub> O = CH <sub>3</sub> O + CH <sub>2</sub> O	9.722E+15	-1.10	2.064E+04	†

Continued

**Table I** Continued

No.	Reaction	A	n	E <sub>a</sub>	Reference
47	CH <sub>3</sub> OCHO + O = CH <sub>3</sub> OCO + OH	2.350E+05	2.50	2.230E+03	†
48	CH <sub>3</sub> OCHO + H = CH <sub>3</sub> OCO + H <sub>2</sub>	4.550E+06	2.00	5.000E+03	†
49	CH <sub>3</sub> OCHO + CH <sub>3</sub> = CH <sub>3</sub> OCO + CH <sub>4</sub>	7.550E-01	3.46	5.481E+03	†
50	CH <sub>3</sub> OCHO + CH <sub>3</sub> O = CH <sub>3</sub> OCO + CH <sub>3</sub> OH	5.480E+11	0.00	5.000E+03	†
51	CH <sub>3</sub> OCO = CH <sub>3</sub> O + CO	7.451E+12	-1.76	1.715E+04	†
52	CH <sub>3</sub> OCO = CH <sub>3</sub> + CO <sub>2</sub>	1.514E+12	-1.78	1.382E+04	†

\* This study.

† Reactions taken from Curran et al. [1,2].

<sup>a</sup> Further details about the pressure dependence of this reaction are provided as Supplementary Material.

[30]. Figure 2 shows the results of this new correlation against the experimental data as well as the rate expression used in the mechanism of Curran et al. [1,2]. The present rate expression exhibits strong temperature dependence, similar to the theoretical work of Wu et al. [46], although their rate is consistently lower than the experimental data (by approximately a factor of 3) and the present result. The present recommendation is a factor of 3.5 higher than that put forth by Curran et al. [1,2] at 1000 K.

The change in the rate expression of reaction (R2) is substantial; however, it is well justified by considering similar reactions for which rate measurements are better established. One such reaction is the H abstraction from acetone (CH<sub>3</sub>COCH<sub>3</sub>) by methyl. On the basis of the measurements of Mousavipour and Pacey [47], the rate of this reaction at 1000 K is a factor of 1.2 faster than the measurement of Held et al. [31] for reaction (R2). However, the primary hydrogen bond dissociation energy is higher for acetone than that for dimethyl ether by about 1 kcal/mol. One can thus reasonably expect the rate expression for reaction (R2) to be faster than the analogous acetone reaction. One should also

note that Held et al. [31] reported rate values for (R2) at 1005 K with considerably smaller uncertainty estimates than Pacey [30]. Held et al., however, did not measure the rate directly but relied on a computer simulation where a kinetic mechanism was used to match experimentally observed CH<sub>4</sub>, C<sub>2</sub>H<sub>6</sub>, and CH<sub>3</sub> concentrations. The determination of the rate of (R2) relied heavily on the rate of the methyl recombination reaction, which Held et al. note at the time of their work was only reliable within a factor of 3. Moreover, in the same study, Held et al. also estimated the rate of H abstraction from formaldehyde by methyl and reported a value which is nearly an order of magnitude lower than other more recent measurements. Consequently, the uncertainty estimates of Held et al. [31] are questionable. Finally, it should be emphasized that, while we accept the present estimate for (R2) rate parameters in our mechanism, it clearly needs further and rigorous investigation at temperatures above 900 K.

Hydrogen abstraction from DME by OH (CH<sub>3</sub>OCH<sub>3</sub> + OH = CH<sub>3</sub>OCH<sub>2</sub> + H<sub>2</sub>O (R3)) is also an important reaction affecting fuel consumption. Tranter and Walker [48] studied reaction (R3) experimentally at 753 K and their data are consistent with the recent experimental work of Bonard et al. [49] conducted at 295–660 K. The rate constant correlation presented by Tranter and Walker [48] was used in the present model, and it exhibits stronger temperature dependence than the correlation used by Curran et al. [1,2]. Tranter and Walker [48] also studied H abstraction from DME by H (CH<sub>3</sub>OCH<sub>3</sub> + H = CH<sub>3</sub>OCH<sub>2</sub> + H<sub>2</sub> (R4)), and this rate correlation was also adopted in the present mechanism. It is about a factor of 1.5 higher than that appearing in the model of Curran et al. [1,2] at 1000 K.

The termination reaction between formyl and methyl radicals, HCO + CH<sub>3</sub> = CO + CH<sub>4</sub>, is also an important reaction in DME oxidation/pyrolysis due to the considerable amounts of HCO and CH<sub>3</sub> present in the system. The temperature-independent rate constant in the original model of Curran et al. [1,2]

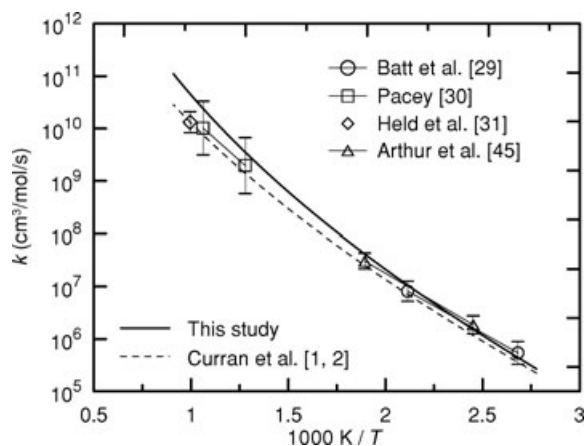


**Figure 2** Arrhenius plots of rate constant expressions for CH<sub>3</sub>OCH<sub>3</sub> + CH<sub>3</sub> = CH<sub>3</sub>OCH<sub>2</sub> + CH<sub>4</sub>.

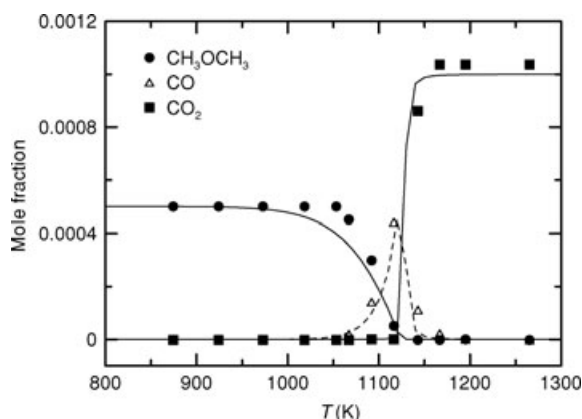


**Figure 3** Reactivity profiles obtained in a flow reactor [59] compared against model predictions ( $P = 1$  atm, 500 ppm DME, 3000 ppm  $O_2$ , 3.34%  $H_2O$  in balance  $N_2$ , residence time (s) = 188 K/T). Dashed lines correspond to open symbols.

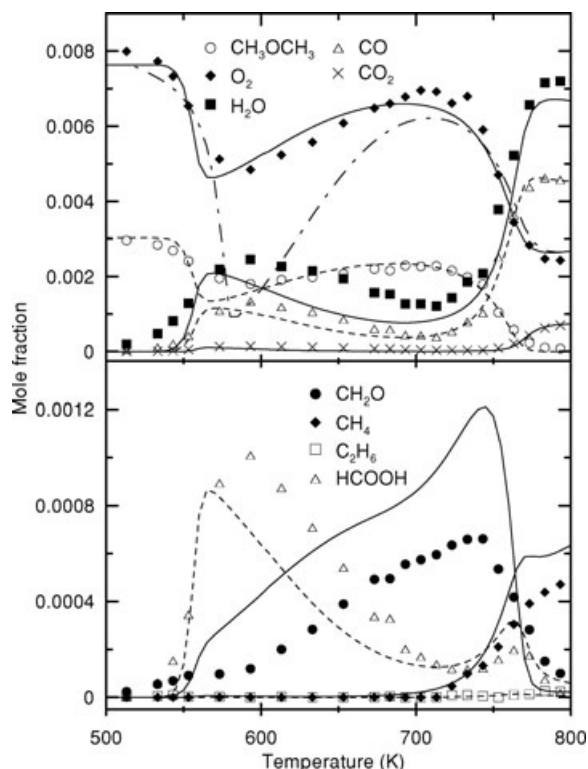


**Figure 4** Measured [2] and computed species profiles in a variable pressure flow reactor ( $P = 12.5$  atm, 3030 ppm DME,  $\phi = 1.19$ , in balance  $N_2$ , residence time = 1.8 s). Dashed lines correspond to open symbols; dash-dot line corresponds to the  $O_2$  profile predicted using the model of Dagaut et al. [5].

is  $1.21 \times 10^{14}$  cm<sup>3</sup>/mol/s. This value is near the collision limit and likely exceeds the high-pressure limit for this reaction. In the present model, we used a rate constant of  $2.65 \times 10^{13}$  cm<sup>3</sup>/mol/s from Mulenko [50], which is also used in GRI-Mech 3.0 [51].

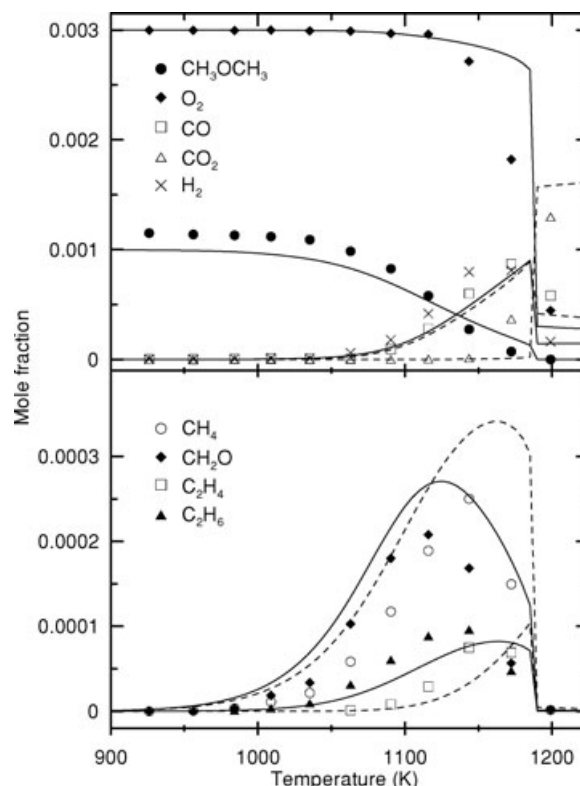


**Figure 5** Jet-stirred reactor species profiles [4] versus model predictions ( $P = 1$  atm, 0.1% DME, 0.3%  $O_2$  in balance  $N_2$ , residence time = 0.1 s). Dashed lines correspond to open symbols.

The low-temperature DME reaction subset from [1,2] was adopted in the present model. Reactions in this subset include chemistry for the formation of formic acid and methyl formate. Formic acid has been shown to be a major intermediate at low temperatures [2,52]; previous modeling efforts [4,5] did not treat these species. A number of reactions in the low-temperature DME oxidation process were updated in this study to improve agreement between model predictions and experimental targets. The low-temperature sequence stems from the addition of molecular oxygen to the methoxymethyl radical to form methoxymethyl-peroxy ( $CH_3OCH_2O_2$ ),  $CH_3OCH_2 + O_2 = CH_3OCH_2O_2$  (R11). The rate for this reaction remains unchanged from the work of Curran et al. [1,2] and is set to  $2.0 \times 10^{12}$  cm<sup>3</sup>/mol/s. This value approaches the room temperature measurement of Sehested et al. [53]. The methoxymethyl radical may also decompose through  $\beta$ -scission to form formaldehyde and the methyl radical  $CH_3OCH_2 = CH_2O + CH_3$  (R10). In the present model, the rate of reaction (R10) has been reduced by approximately 25% to obtain good agreement with experimental results,

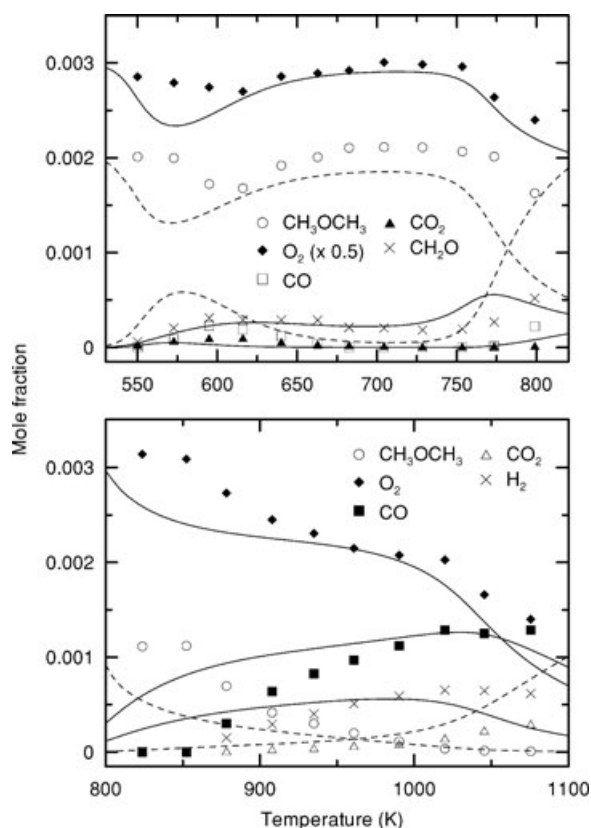


**Figure 6** Jet-stirred reactor species profiles [5] versus model predictions ( $P = 10$  atm; top: 0.2% DME, 0.6%  $O_2$ ; bottom: 0.1% DME, 0.3%  $O_2$  in balance  $N_2$ ; residence time = 1 s). Dashed lines correspond to open symbols.

especially at intermediate temperatures (around 800 K). This rate reduction is well within the uncertainty estimates of Loucks and Laidler [54] from which the rate expression was originally taken [2]. Recently, Li et al. [55] have proposed a new rate for the decomposition reaction (R10) based on ab initio and density-functional theory studies; their calculated rate, however, is approximately a factor of 3 faster than the rate currently employed over the temperature range of interest in this study.

Perhaps the most important step at low temperatures is the isomerization of the methoxymethylperoxy radical  $CH_3OCH_2O_2 = CH_2OCH_2O_2H$  (R15). The hydroperoxy-methoxymethyl radical formed ( $CH_2OCH_2O_2H$ ) may undergo  $\beta$ -scission releasing two formaldehyde molecules and a hydroxyl radical ( $CH_2OCH_2O_2H = CH_2O + CH_2O = OH$  (R17)), or it can react with molecular oxygen to form the  $O_2CH_2OCH_2O_2H$  radical ( $CH_2OCH_2O_2H + O_2 = O_2CH_2OCH_2O_2H$  (R18)). Similar to methoxymethylperoxy, the  $O_2CH_2OCH_2O_2H$  radical also isomerizes, yielding a hydroxyl molecule and a stable

carbonyl-hydroperoxide molecule ( $O_2CH_2OCH_2O_2H = HO_2CH_2OCHO + OH$  (R19)), which, in turn, decomposes releasing an additional OH radical ( $HO_2CH_2OCHO = OCH_2OCHO + OH$  (R20)). The above sequence (R15, R18–R20) provides chain branching at low temperatures (below 700 K). As temperature increases,  $\beta$ -scission of the  $CH_2OCH_2O_2H$  radical (R17) dominates leading to the negative temperature coefficient (NTC) region as the reactivity of the system decreases since only one reactive hydroxyl molecule is released. Rate expressions for kinetic steps (R15, R17–R19) remain unchanged from [1,2]. In the present model, the rate of reaction (R20) was increased by approximately 50% from the value proposed by Curran et al. [1,2]. The rate expression employed here for (R20) is different from the values published by Sahetchian et al. [56] for the decomposition of organic hydroperoxides. This change, however, allowed for better agreement with experimental results at low temperatures, especially in terms of ignition delay measurements. Curran et al. [57] showed that shock tube ignition delay times are most sensitive to reaction (R20) at temperatures below 650 K, with essentially no sensitivity at higher temperatures. Furthermore, Liu et al. [52] have shown that at temperatures below 650 K accumulation of hydroperoxymethyl formate ( $HO_2CH_2OCHO$ ) did not occur in their experiments to the extent predicted by the model of Curran et al. [1,2], thus supporting the present increase in the rate of reaction (R20), which promotes the removal of this species.

One further modification of the low-temperature subset involves the rate of H abstraction from the fuel by the hydroperoxyl radical ( $CH_3OCH_3 + HO_2 = CH_3OCH_2 + H_2O_2$  (R6)), to increase the reactivity of the system at temperatures above 750 K. The original rate expression [1,2] for reaction (R6) was taken from Walker [58] based on his recommendation for abstraction of secondary H atoms from alkane molecules by  $HO_2$  radicals (i.e.,  $2.83 \times 10^{12} \exp(-17.69 \text{ kcal}/RT) \text{ cm}^3/\text{mol/s}$  per available H atom). In this study, the activation energy for reaction (R13) was adjusted downward by 1 kcal whereas the A-factor was increased by approximately 18% (i.e.,  $3.33 \times 10^{12} \exp(-16.69 \text{ kcal}/RT) \text{ cm}^3/\text{mol/s}$  per available H atom). These revisions are within quoted uncertainty estimates [58].

## RESULTS AND DISCUSSION

The DME model described above was compared with pyrolysis and oxidation results in various experimental devices. Figures 3–6 show species profiles as a function of temperature from a variety of



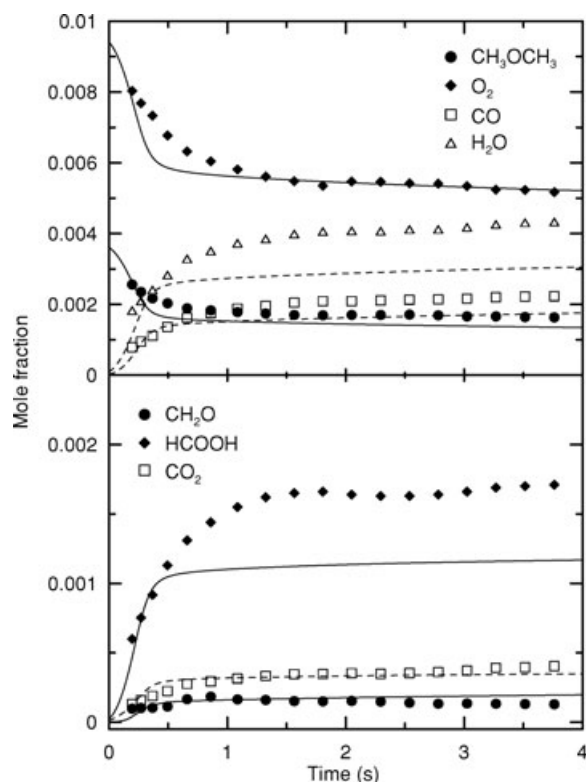


**Figure 7** Comparison of experimental [2] (symbols) and computed (lines) species profiles during DME oxidation in a flow reactor ( $P = 18$  atm,  $T = 580$  K,  $\phi = 1.16$ , initial DME concentration 3700 ppm in  $N_2$ ). Model predictions are shifted by  $-0.27$  s. Dashed lines correspond to open symbols.

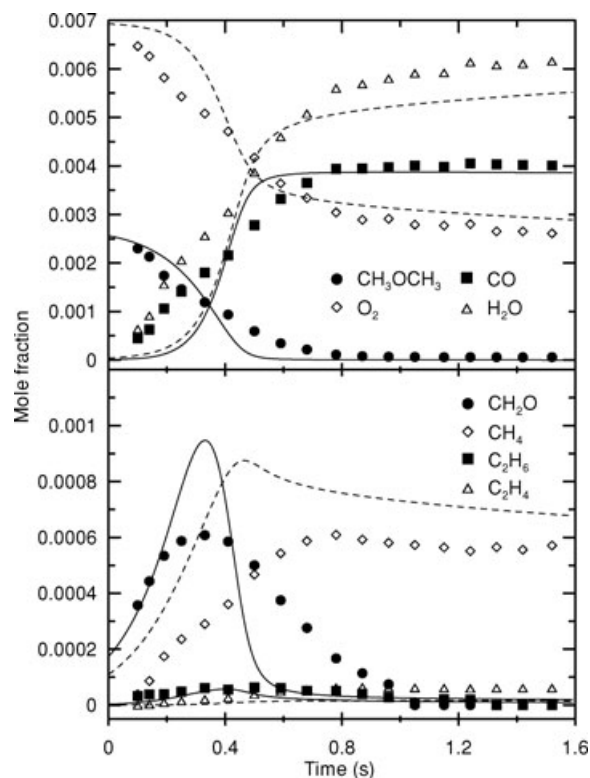


**Figure 8** Comparison of experimental [2] (symbols) and computed (lines) species profiles during DME oxidation in a flow reactor ( $P = 12$  atm,  $T = 849$  K,  $\phi = 1.17$ , initial DME concentration 2730 ppm in  $N_2$ ). Model predictions are shifted by  $-0.35$  s. Dashed lines correspond to open symbols.

reactor systems [2,4,5,59] against model predictions in the low- and high-temperature regimes for different fuel/oxidizer concentrations at atmospheric as well as high pressures. Model results were obtained by assuming isobaric and adiabatic systems. The methods used here to properly compare model computations with experimental data are described in detail in the Supplementary Material accompanying this paper. Figure 3 shows comparisons with the high-temperature data reported by Alzueta et al. [59]. The current model predicts the shape of the curves and shows good agreement when considering the temperature for complete DME consumption (i.e., peak CO production). Figure 4 depicts simulated species profiles against data obtained in the Princeton VPFR by Curran et al. [2] at a mean residence time of 1.8 s for  $500 < T < 800$  K. There is good agreement between model and experiments, and the model clearly captures the NTC behavior observed experimentally. Not surprisingly, in this low to intermediate temperature regime, the present model yields similar agreement as that obtained by Curran et al. [2]. Figures 5 and 6 show simulations against

data obtained in a jet-stirred reactor [4,5] for stoichiometric DME/ $O_2/N_2$  mixtures at 1 and 10 atm, respectively. Relatively good agreement is observed between experiments and predictions. At 1 atm (Fig. 5), the present mechanism predicts fast DME consumption (considering the  $O_2$  profile) to begin at approximately 20 K higher than observed experimentally. At 10 atm (Fig. 6), the model predicts more reactivity at temperatures exceeding 775 K; however, the profile shapes are well reproduced. The reactivity trends observed in the jet-stirred reactor, however, are somewhat inconsistent with those obtained in the flow reactor at similar pressure and temperatures (Fig. 4). In fact, employing the model of Dagaut et al. [5] (which was developed based on the jet-stirred reactor data shown in Figs. 5 and 6) to simulate the data of Fig. 4 yields large disparities as shown by the oxygen profile in Fig. 4 (dashed line).

Representative comparisons of product species measured in the VPFR [1,2] and predicted by the present model are shown in Figs. 7–10 for both oxidation and pyrolysis conditions. The model predicts well the VPFR data for major species (e.g., DME,  $O_2$ , CO,

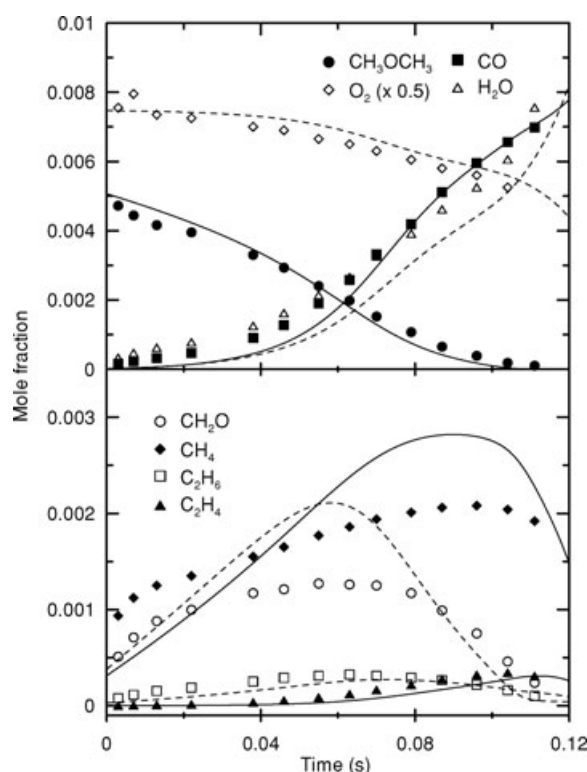


**Figure 9** Comparison of experimental [1] (symbols) and computed (lines) species profiles during DME oxidation in a flow reactor ( $P = 1.0$  atm,  $T = 1084$  K,  $\phi = 1.06$ , initial DME concentration 5270 ppm in  $N_2$ ). Model predictions are shifted by  $-12$  ms. Dashed lines correspond to open symbols.

$H_2O$ ) and even for trace intermediates at stoichiometric (Figs. 7–9) and lean conditions. For fuel-rich and pyrolysis (Fig. 10) cases, the agreement with fuel/oxygen consumption remains; however, minor species and intermediates are predicted less satisfactorily.

One of the main discrepancies observed in Figs. 7–10 is in the measured and predicted methane and, to a lesser extent, formaldehyde profiles. Sensitivity analyses were performed to determine the reactions that strongly influence the DME pyrolysis/oxidation system. Figure 11 shows the important reactions for,  $CH_4$ ,  $CH_2O$ , and  $H_2O$  with their sensitivity coefficients calculated when 80% fuel is consumed for a  $\phi = 3.16$  case at 1 atm. Under these conditions, the concentration of these species is all very sensitive to fuel decomposition (R1), the reaction of fuel with the methyl radical (R2), and several other reactions involving methyl radical, including  $CH_3 + CH_3 (+M) = C_2H_6 (+M)$ ,  $CH_2O + CH_3 = CH_4 + HCO$ ,  $CH_3 + HO_2 = CH_4 + O_2$ ,  $CH_3 + HO_2 = CH_3O + OH$ , as well as reactions related to the formaldehyde oxidation submechanism. Improving the model agreement with methane and formaldehyde, thus, would require further work at this molecular in-

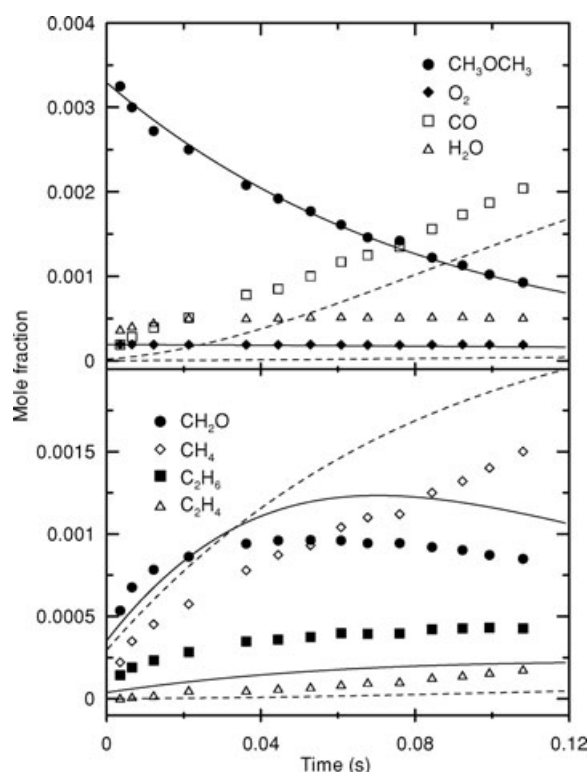


**Figure 10** Comparison of experimental [1] (symbols) and computed (lines) species profiles during DME near-pyrolysis in a flow reactor ( $P = 1.0$  atm,  $T = 1118$  K, initial DME concentration 3740 ppm in  $N_2$ ,  $O_2$  concentration 190 ppm). Model predictions are shifted by  $-19$  ms. Dashed lines correspond to open symbols.

termediate species level, which may alter predictions previously obtained for these systems (e.g., formaldehyde, see [42]).

Results from the present pyrolysis experiments are shown in Fig. 12. Previously [1,2], no pyrolysis results were reported at the pressure and temperature conditions studied here. As noted above, the present theoretical results for the decomposition reaction (R1) show a higher degree of falloff than the rate used by Curran et al. [1,2]. The experiments performed in this study lend further support to this claim. As seen in Fig. 12, modeling performed using the mechanisms of Curran et al. [1,2] and Dagaut et al. [5] shows species profile evolutions that are considerably slower than experimental results. The present model, on the other hand, shows excellent agreement with experiments when considering DME and  $CH_4$  profiles, with CO and  $CH_2O$  being under- and over-predicted, respectively. Model computations were compared against pyrolysis data using the approach of Li et al. [60], also discussed in the Supplementary Material. Figure 13 shows results obtained from sensitivity analyses under

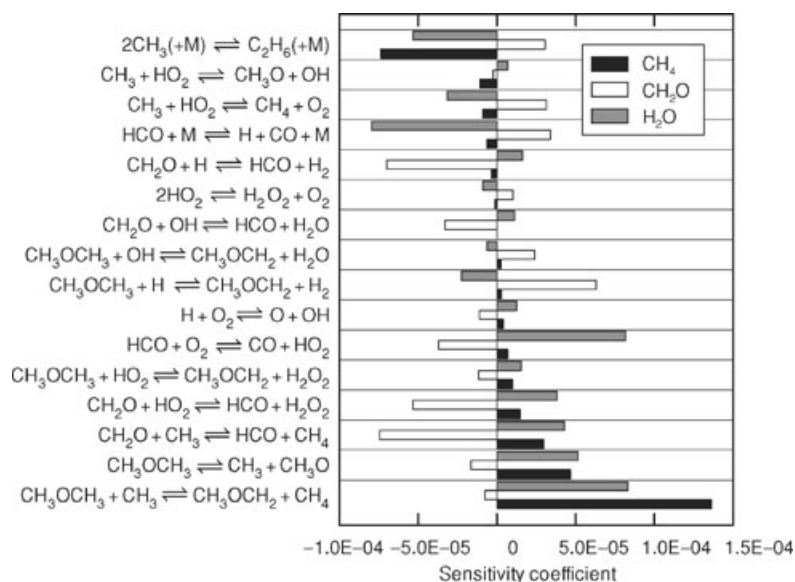


**Figure 11** Sensitivity coefficients of selected species for DME oxidation in a flow reactor (initial conditions:  $P = 1.0$  atm,  $T_i = 1080$  K,  $\phi \approx 3.4$ , DME = 5160 ppm in  $\text{N}_2$ ; see Fig. 9) at 80% fuel consumption.

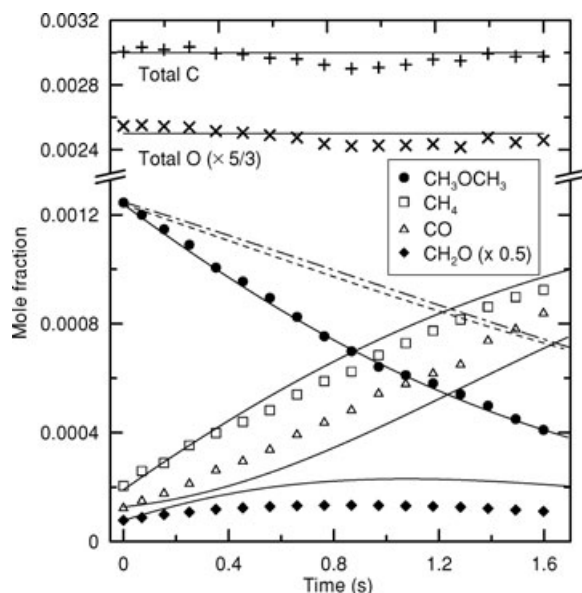


**Figure 12** Measured species profiles in a flow reactor under pyrolysis conditions ( $P = 10$  atm,  $T = 980$  K, 1500 ppm DME in balance  $\text{N}_2$ ). Solid lines are predictions using the present model, dashed lines are calculated DME profiles using the model of Curran et al. [1,2], and dash-dot lines denote the DME predictions from the model of Dagaut et al. [5]. For completeness, carbon and oxygen balances considering all experimentally identified species are shown. Computations and experiments are compared using the initialization technique described in the Supplementary Material that lists the initialization conditions used for computations.

the present pyrolysis conditions. The argument could be made that the agreement seen in Fig. 12 for the present mechanism is a direct result of the higher rate chosen for reaction (R2) as this reaction is particularly sensitive. In fact, introducing the present rate for reaction (R2) into the model of Curran et al. [1,2] improves its agreement against the present pyrolysis results. However, agreement with low-pressure data is substantially degraded since the DME decomposition rate chosen in the study of Curran et al. exhibits a much smaller falloff, as mentioned above. Thus, the theoretical treatment of reaction (R1) undertaken in this study allows the model described herein to reconcile both low- and high-pressure experimental results.

The chemical kinetic mechanism was also used to simulate experimental shock tube results [5,6]. Modeling was performed assuming isochoric and adiabatic conditions. Figure 14 shows a comparison of the current model predictions with the data of Pfahl et al. [6]. There is good agreement between experiments and computations. However, the model overpredicts ignition delays at lower temperatures. Figure 15 shows predicted ignition delay times according to the peak  $[\text{CO}] \times [\text{O}]$  in the temperature range of 1200–1600 K and at 3.5 bar against the measurements of Dagaut et al. [5]. Reasonable agreement between prediction and experiment is achieved for all equivalence ratios, although predictions are somewhat larger at lower temperatures and exhibit larger activation energies. Both

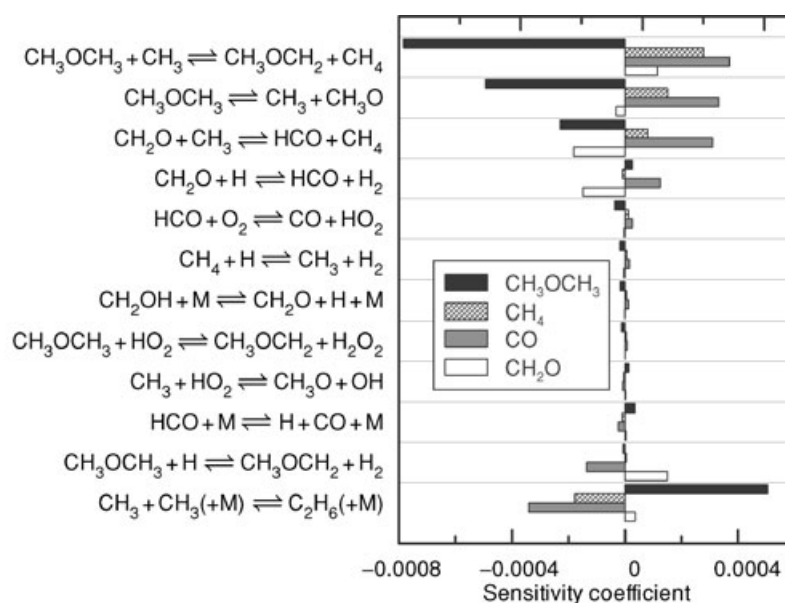


**Figure 13** Sensitivity coefficients of selected species for DME pyrolysis in a flow reactor (Initial conditions  $P = 10$  atm,  $T_i = 980$  K, 1500 ppm DME in  $\text{N}_2$ ) at 60% fuel consumption.

predicted and experimental ignition delay times decrease at lean conditions. For comparison, ignition delays calculated using the model of Fischer et al. [1,2] are also shown for  $\phi = 2$  in Fig. 15. The shorter ignition delays predicted by the model are a direct result of the higher rate constant for reaction (R1) used by Fischer et al. (see Fig. 1) at the temperatures and pressure of interest. It has been shown, however, that the rate constant used by Fischer et al. [1,2] cannot predict present high-pressure pyrolysis results (see Fig. 12). In a recent study by Bowman et al. [61], DME ignition was studied in a shock tube under conditions similar to those of Dagaut et al. [5]. Emission from

electronically excited CH as well as OH radicals was used to determine ignition delay rather than  $\text{CO}_2$  emission [5]. Figure 16 shows predictions from the present DME model against the measurements of Bowman et al. [61]. Agreement, both in terms of absolute ignition delay values and activation energies, is considerably better than in the comparisons with shock tube ignition delay data presented in Fig. 15.

Figures 17 and 18 show results obtained from sensitivity analyses performed using the present model under the conditions of Pfahl et al. [6] and Dagaut et al.

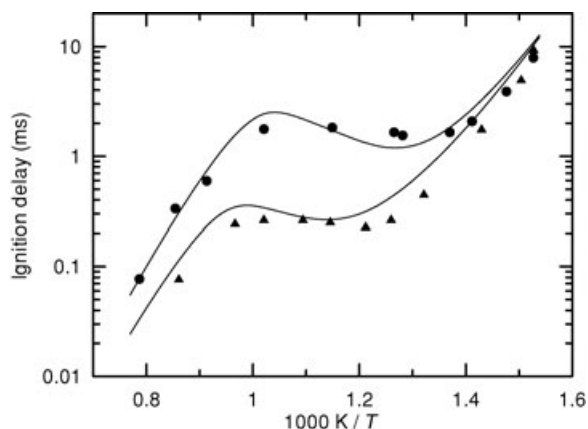


**Figure 14** Stoichiometric DME/air ignition delay measurements [6] against model predictions. Circles and triangles denote measurements at 13 and 40 bar, respectively.

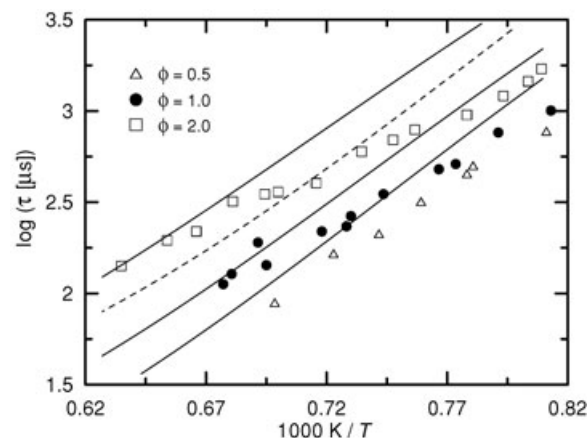


**Figure 15** Comparison of experimental (symbols) [5] and computed (lines) ignition delay times for DME/ $\text{O}_2$ /Ar mixtures in a shock tube at 3.5 bar and 1% DME concentration. Dashed line represents computed results for  $\phi = 2$  using the model of Fischer et al. [1,2].

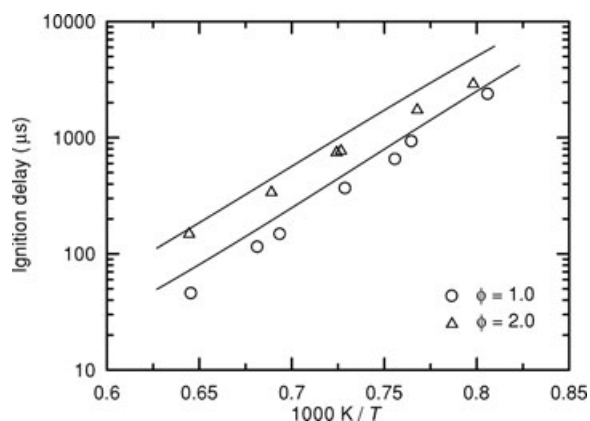


**Figure 16** Ignition delay times for DME/O<sub>2</sub>/Ar mixtures in a shock tube at and average pressure of 1.8 atm and 1% DME concentration. Symbols are the experimental measurements of Bowman et al. [61], and lines show model predictions.

[5], respectively. Figure 17 shows how the various low-temperature reactions influence DME/air ignition. At low temperatures (i.e., 650 K) and through the NTC region, the isomerization of the methoxymethyl-peroxy radical (R15) is important. Clearly, the decomposi-

tion of the hydroperoxy-methoxymethyl radical (R17) gains sensitivity along with molecular oxygen addition to CH<sub>2</sub>OCH<sub>2</sub>O<sub>2</sub>H (R18) and the decomposition of the methoxymethyl radical (R10) within the NTC regime. As temperature increases beyond 900 K, reactions such as methyl radical recombination and H abstraction from DME by methyl (R2) become important. At high temperatures, as shown in Fig. 18, ignition delay time is very sensitive to the fuel decomposition reaction (R1) and to several reactions involving the methyl radical and formaldehyde.

Chemical species profiles have been measured in burner-stabilized flames at atmospheric pressure for DME/air, using gas chromatography and FTIR spectroscopy [8], and for DME/O<sub>2</sub>/Ar at low pressure (4 kPa) using a molecular beam mass spectrometer and laser-induced fluorescence (LIF) [9]. As shown in Fig. 19 for the low-pressure flame, the model performs well in reproducing the major stable species, such as DME, O<sub>2</sub>, CO, CO<sub>2</sub>, H<sub>2</sub>O, and H<sub>2</sub>. Minor species such as CH<sub>4</sub> and CH<sub>2</sub>O are also well predicted by the model. The predicted and measured acetylene (C<sub>2</sub>H<sub>2</sub>) profile shapes are in good agreement, but the magnitude of the experimental data is significantly higher than that

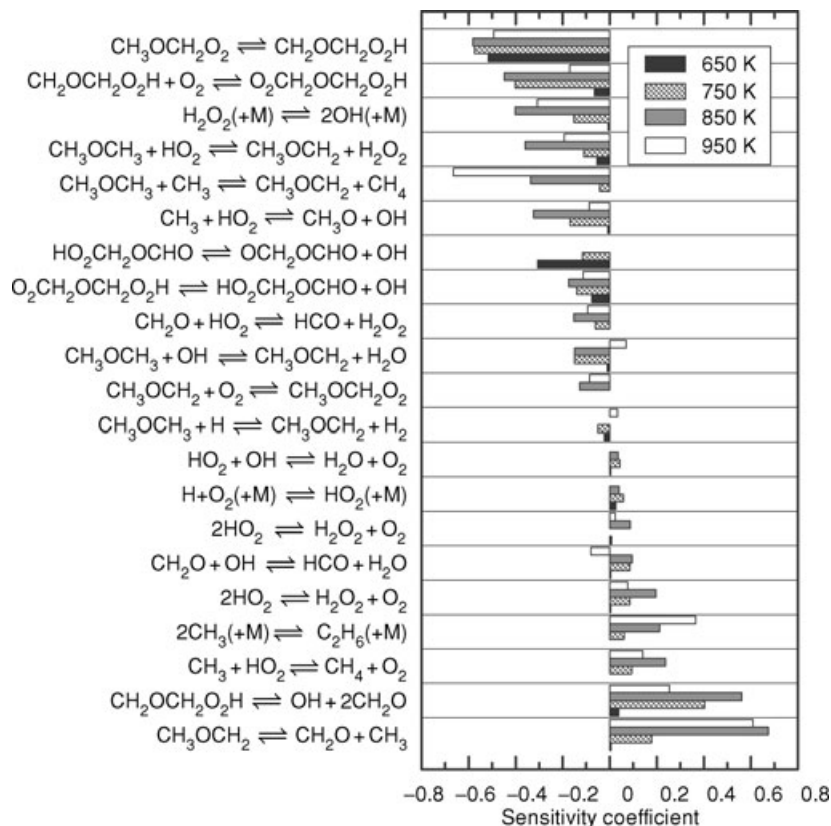


**Figure 17** Ignition delay time sensitivity to reaction rates for stoichiometric DME/air mixtures in a shock tube at 13 bar.

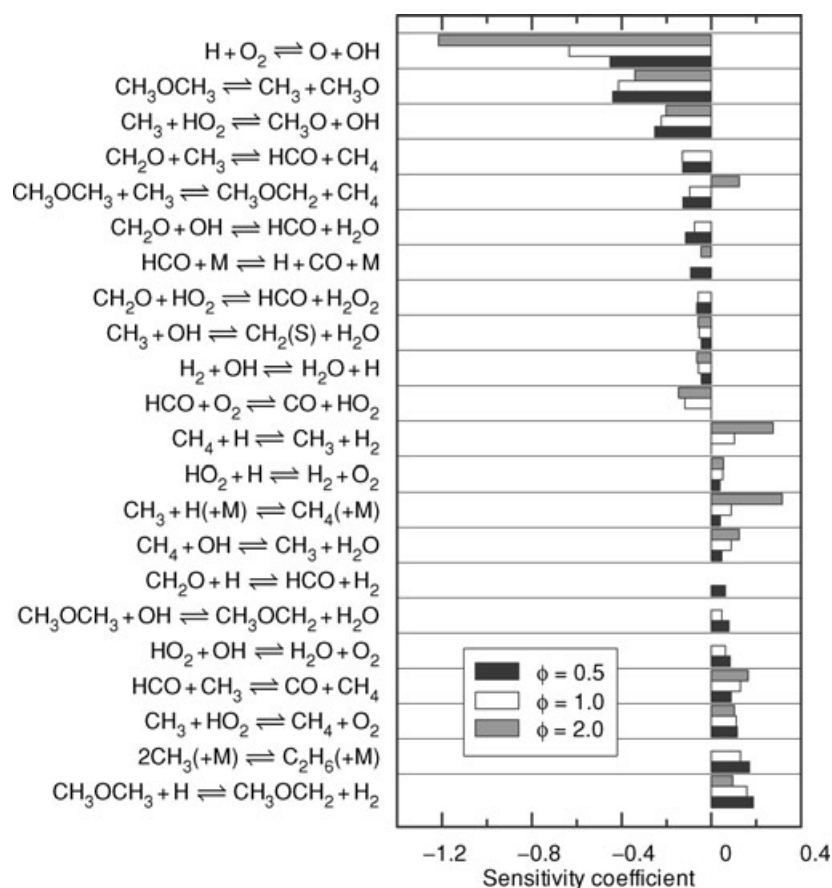


**Figure 18** Ignition delay time sensitivity to reaction rates for DME/O<sub>2</sub>/Ar mixtures in a shock tube at 1400 K and 3.5 bar.

predicted. For the OH radical, the model reproduces well the shape of the profile, however, discrepancies are observed at postflame equilibria. This disagreement is most likely caused by OH calibration in the LIF experiments, where the values from equilibrium calculations were used to calibrate OH. Recently, Ruscic et al. [62] studied the heat of formation of the OH radical both experimentally and theoretically and recommended a value of 8.91 kcal/mol at 298 K, which is in excellent agreement with the recent experimental result of 8.92 kcal/mol by Herbon et al. [63]. The heat of formation value presented by Ruscic et al. [62] was used in the current mechanism. It is significantly different from the one used in the CHEMKIN [64] database, which was likely the value used in LIF calibrations [9]. As shown by the dashed line in Fig. 19, changing the OH thermochemical data in the present model back to the value listed in the CHEMKIN database enables the model to predict the OH concentration at equilibrium. Figure 20 shows comparisons between measured and computed species profiles for atmospheric DME/air flames. Again, generally good agreement between model and experiment is observed for major species (DME, O<sub>2</sub>,

CO, and CO<sub>2</sub>). Intermediate species, such as C<sub>2</sub>H<sub>4</sub> and C<sub>2</sub>H<sub>6</sub>, are also correctly reproduced by the model. Some deficiencies exist for CH<sub>2</sub>O and CH<sub>4</sub>. New data from low-pressure stabilized burner flames have recently been obtained and also compare favorably with the present model predictions. Those comparisons are discussed in more detail elsewhere [65].

Predicted laminar flame speeds for room temperature DME/air mixtures are shown in Fig. 21 compared with experimental measurements for a range of pressures. For both burner-stabilized (above) and flame speed calculations, the PREMIX code [66] was used employing the standard CHEMKIN transport package [67] with Soret effects and multicomponent diffusion included. To assure a fully converged prediction, a minimum of 1000 grid points was imposed in the PREMIX calculations. Similar to other fuels (e.g., [11]), the experimental data exhibit significant scatter (a difference of up to approximately 20% in some cases). The laminar flame speed data from our previous study [68] are consistently higher than other measurements available in the literature [10,11,69]. As can be seen in Fig. 21, the present model reproduces well the laminar

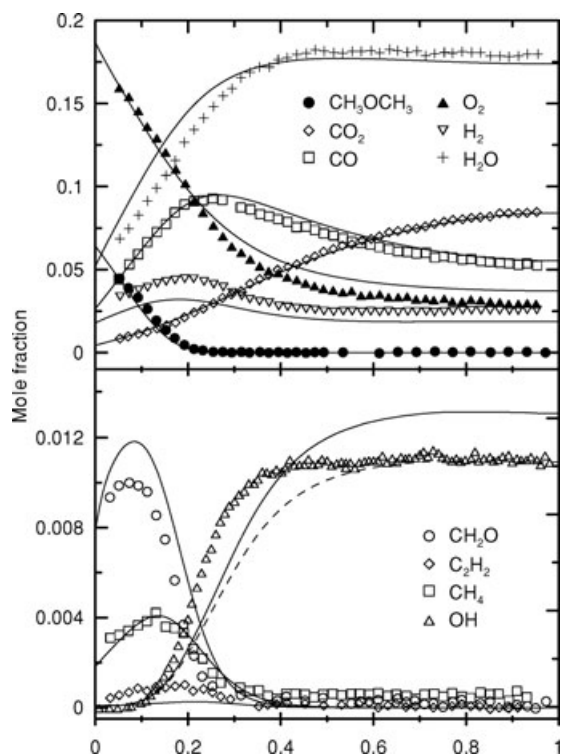


**Figure 19** Comparison of experimental [9] (symbols) and computed (lines) species profiles in a DME- $\text{O}_2$ -Ar burner-stabilized flame ( $P = 4 \text{ kPa}$ ,  $\phi = 0.98$ ).

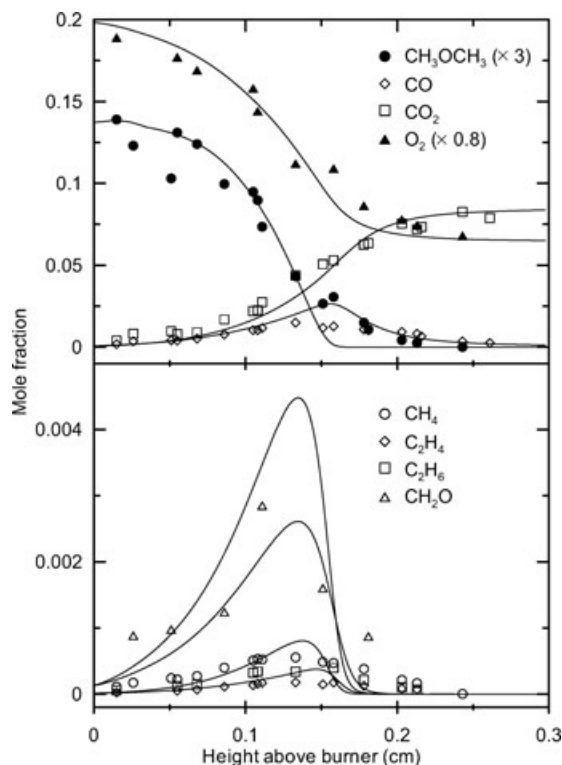


**Figure 20** Comparison of experimental [8] (symbols) and computed (lines) species profiles in DME-air burner-stabilized flame ( $P = 1.0 \text{ atm}$ ,  $\phi = 0.67$ ).

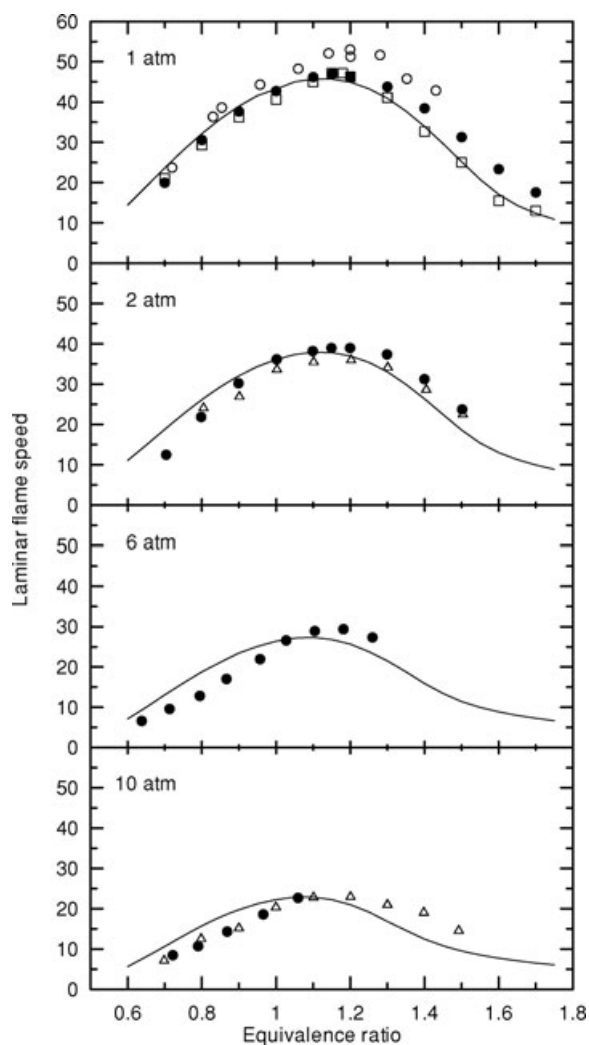


**Figure 21** Laminar flame speeds of DME/air mixtures at different pressures (1, 2, 6, and 10 atm). Filled symbols represent the experimental data of Qin and Ju [11]; open circles: Zhao et al. [68]; open squares: Daly et al. [10]; open triangles: Law and Jomaas. [69]; lines: model prediction.

flame speed at atmospheric pressure, yet the agreement somewhat degrades as pressure increases. The model, however, captures the dependence of the laminar flame speed on pressure, which is important as this dependence is a measure of the overall reaction order of the system [70]. The sensitivity spectrum for DME/air flames is similar for all pressures and it exhibits the features typically seen and well documented for small hydrocarbon flames, and the results are qualitatively similar to those obtained using the model of Curran et al. [2] (see [68]). Figure 22 shows the sensitivity results for laminar flame speed at 10 atm and 298 K. The spectrum is dominated by the main chain branching reaction,  $\text{H} + \text{O}_2 = \text{OH} + \text{O}$ , formyl decomposition,

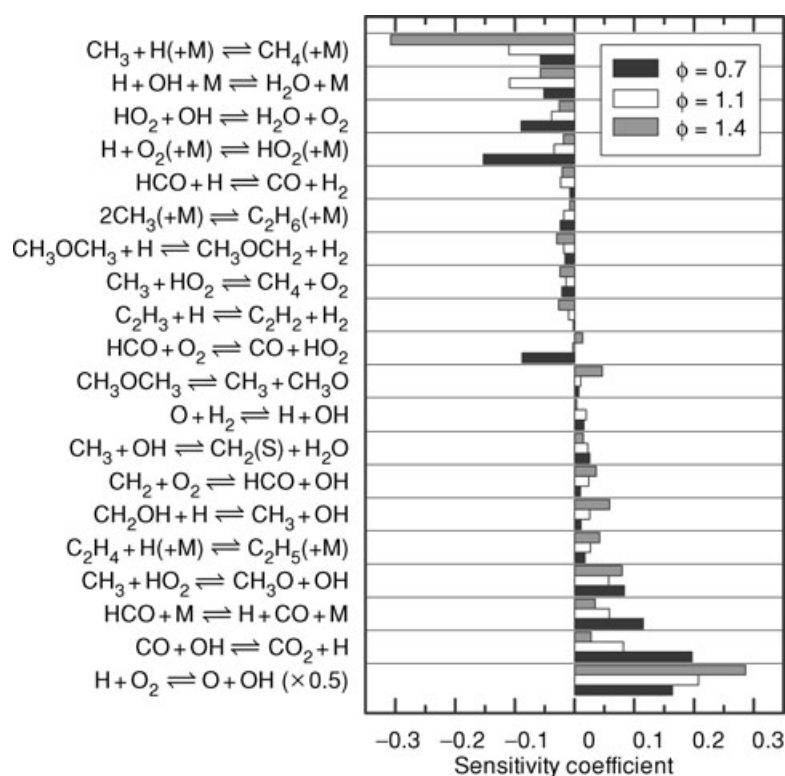


**Figure 22** Normalized sensitivity coefficients of DME/air flame speeds at 298 K and 10 atm calculated using the present kinetic model. Note that the sensitivity coefficient for reaction  $\text{H} + \text{O}_2 = \text{O} + \text{OH}$  has been reduced by half to better display the rest of the spectrum.

$\text{HCO} + \text{M} = \text{CO} + \text{H} + \text{M}$ , and CO oxidation,  $\text{CO} + \text{OH} = \text{CO}_2 + \text{H}$ . The reactions that are specific to DME and contribute noticeably are only the unimolecular decomposition of DME,  $\text{CH}_3\text{OCH}_3 = \text{CH}_3 + \text{CH}_3\text{O}$  (R1), and H abstraction from DME by the H atom,  $\text{CH}_3\text{OCH}_3 + \text{H} = \text{CH}_3\text{OCH}_2 + \text{H}_2$  (R4). Finally, the present model has recently been used to study the effect of DME addition on the burning properties of methane flames. As opposed to previous efforts [1,2], the present model is able to predict flame speeds for pure methane as well as for methane/DME blends. Further details and comparisons can be found in [71].

## CONCLUSION

A comprehensive DME pyrolysis and oxidation model based on the hierarchical nature of reacting systems has been developed to reflect new developments in small molecule and radical kinetics and thermochemistry. The thermal decomposition of DME has been given special attention in this work as this reaction is the most important initiation step, and subsequent validation of the pyrolysis and oxidation model and, in particular, the abstraction reactions involving DME are

substantially influenced by the description of the DME decomposition. DME thermal decomposition was studied theoretically by using the RRKM/master equation approach. The newly calculated rate coefficient is significantly different than values used previously. However, new pyrolysis experiments performed at a pressure of 10 atm and at temperatures near 1000 K show very good agreement with calculations performed using the model described herein. The new model was used to simulate experimental results obtained in flow reactors, jet-stirred reactors, shock tubes, and burner-stabilized flames. Overall good agreement is obtained under all conditions, supporting the reliability of the present mechanism. Laminar flame speed predictions also reasonably agree with available experimental data.

Sensitivity analyses suggest the need for further model refinement for reactions involving the  $\text{C}_1$  level submechanism, especially formaldehyde oxidation. While it is possible to further improve the agreement between the model predictions and available data by adjusting less established rate coefficients, the present agreement appears to be acceptable for a majority of model uses. Modifications in kinetics and thermochemistry should not be performed based upon improving this agreement without investigating the



result of the changes in predictions of fundamental kinetics observations used in initially validating the model and against flame speed measurements for other simple fuels.

The authors would like to thank Prof. H. Curran for helpful discussions.

## BIBLIOGRAPHY

- Fischer, S. L.; Dryer, F. L.; Curran, H. J. *Int J Chem Kinet* 2000, 32, 713–740.
- Curran, H. J.; Fischer, S. L.; Dryer, F. L. *Int J Chem Kinet* 2000, 32, 741–759.
- Curran, H. J. Personal communication, 2004.
- Dagaut, P.; Boettner, J.-C.; Cathonnet, M. *Proc Combust Inst* 1996, 26, 627–632.
- Dagaut, P.; Daly, C.; Simmie, J. M.; Cathonnet, M. *Proc Combust Inst* 1998, 27, 361–369.
- Pfahl, U.; Fieweger, K.; Adomeit, G. *Proc Combust Inst* 1996, 26, 781–789.
- Zheng, X. L.; Lu, T. F.; Law, C. K.; Westbrook, C. K.; Curran, H. J. *Proc Combust Inst* 2005, 30, 1101–1109.
- Kaiser, E. W.; Wallington, T. J.; Hurley, M. D.; Platz, J.; Curran, H. J.; Pitz, W. J.; Westbrook, C. K. *J Phys Chem A* 2000, 104, 8194–8206.
- McIlroy, A.; Hain, T. D.; Michelsen, H. A.; Cool, T. A. *Proc Combust Inst* 2000, 28, 1647–1653.
- Daly, C. A.; Simmie, J. M.; Würmel, J.; Djebaili, N.; Paillard, C. *Combust Flame* 2001, 125, 1329–1340.
- Qin, X.; Ju, Y. *Proc Combust Inst* 2004, 30, 233–240.
- Nash, J. J.; Francisco, J. S. *J Phys Chem A* 1998, 102, 236–241.
- Andersen, A.; Carter, E. A. *Israel J Chem* 2002, 42, 245–260.
- Andersen, A.; Carter, E. A. *J Phys Chem A* 2003, 107, 9463–9478.
- Li, J.; Kazakov, A.; Dryer, F. L. *J Phys Chem A* 2004, 108, 7671–7680.
- Becke, A. D. *Phys Rev A* 1988, 38, 3098–3100.
- Becke, A. D. *J Chem Phys* 1993, 98, 5648–5652.
- Lee, C.; Yang, W.; Parr, R. G. *Phys Rev B* 1988, 37, 785–789.
- Stephens, P. J.; Devlin, F. J.; Chabalowski, C. F.; Frisch, M. J. *J Phys Chem* 1994, 98, 11623–11627.
- Baboul, A. G.; Curtiss, L. A.; Redfern, P. C.; Raghavachari, K. *J Chem Phys* 1999, 110, 7650–7657.
- Frisch, M. J.; Trucks, G. W.; Schlegel, H. B.; Gill, P. M. W.; Johnson, B. G.; Robb, M. A.; Cheeseman, J. R.; Keith, T.; Petersson, G. A.; Montgomery, J. A.; Raghavachari, K.; Al-Laham, M. A.; Zakrzewski, V. G.; Oritz, J. V.; Foresman, J. B.; Cioslowski, J.; Stefanov, B. B.; Nanyakkara, A.; Challacombe, M.; Peng, C. Y.; Ayala, P. Y.; Chen, W.; Wong, M. W.; Andres, J. L.; Replogle, E. S.; Gomperts, R.; Martin, R. L.; Fox, D. J.; Binkley, J. S.; Defrees, D. J.; Baker, J.; Stewart, J. P.; Head-Gordon, M.; Gonzalez, C.; Pople, J. A. *Gaussian, Inc., Pittsburgh, PA*, 1998.
- Forst, W. *J Phys Chem* 1991, 95, 3612–3620.
- Du, H.; Messier, J. P.; Ogren, P. J. *J Phys Chem* 1996, 100, 974–983.
- Pesa, M.; Pilling, M. J.; Robertson, S. H.; Wardlaw, D. M. *J Phys Chem A* 1998, 102, 8526–8536.
- Gilbert, R. G.; Smith, S. C. *Theory of Unimolecular Recombination Reactions*; Blackwell Scientific Publications: Oxford, UK, 1990.
- Knyazev, V. D.; Slagle, I. R. *J Phys Chem A* 2001, 105, 3196–3204.
- Knyazev, V. D.; Tsang, W. *J Phys Chem A* 2000, 104, 10747–10765.
- Kee, R. J.; Dixon-Lewis, G.; Warnatz, J.; Coltrin, M. E.; Miller, J. A. Technical Report SAND86-8246, Sandia National Laboratories, Albuquerque, NM, 1986.
- Batt, L.; Alvarado-Salinas, G.; Reid, I. A. B.; Robinson, C.; Smith, D. B. *Proc Combust Inst* 1982, 19, 81–87.
- Pacey, P. D. *Can J Chem* 1975, 53, 2742–2747.
- Held, A. M.; Manthorne, K. C.; Pacey, P. D.; Reinholdt, H. P. *Can J Chem* 1977, 55, 4128–4134.
- Aronowitz, D.; Naegeli, D. *Int J Chem Kinet* 1977, 9, 471–479.
- Harding, L. B. In DOE, BBS 25th Annual Combustion Research Conference, Warrenton, VA, 2004.
- Kerr, J. A.; Trotman-Dickenson, A. F. In *Progress in Reaction Kinetics* (Porter, G. ed.); Pergamon Press: Oxford, UK, 1961; pp. 105–129.
- Gerland, L. J.; Bayes, K. D. *J Phys Chem* 1990, 94, 4941–4945.
- Knyazev, V. D.; Slagle, I. R.; Bryukov, M. G. *J Phys Chem A* 2003, 107, 6558–6564.
- Pagsberg, P.; Munk, J.; Sillesen, A.; Anastasi, C. *Chem Phys Lett* 1988, 146, 375–381.
- Wang, B.; Fockenberg, C. *J Phys Chem A* 2001, 105, 8449–8455.
- Cody, R. J.; Payne, W. A. Jr.; Thorn, R. P. Jr.; Nesbitt, F. L.; Iannone, M. A.; Tardy, D. C.; Stief, L. J. *J Phys Chem A* 2002, 106, 6060–6067.
- Barker, J. R.; Benson, S. W.; Mendenhall, G. D.; Goldern, D. M. U.S. NTIS PB Report, 1977.
- Li, J.; Zhao, Z.; Kazakov, A.; Dryer, F. L. *Int J Chem Kinet* 2004, 36, 566–575.
- Li, J.; Zhao, Z.; Kazakov, A.; Chaos, M.; Dryer, F. L.; Scire, J. J., Jr. *Int J Chem Kinet* 2007, 39, 109–136.
- Li, J. Ph.D. thesis, Department of Mechanical and Aerospace Engineering, Princeton University, Princeton, NJ, 2004.
- Li, J.; Kazakov, A.; Chaos, M.; Dryer, F. L. In *Proceedings of the 5th U.S. National Combustion Meeting 2007*, Paper C26.
- Arthur, N. L.; Gray, P.; Herod, A. A. *Can J Chem* 1969, 47, 1347–1350.
- Wu, J. Y.; Liu, J. Y.; Li, Z. S.; Huang, X. R.; Sun, C. C. *J Comp Chem* 2003, 24, 593–600.
- Mousavipour, S. H.; Pacey, P. D. *J Phys Chem* 1996, 100, 3573–3579.

48. Tranter, R. S.; Walker, R. W. *Phys Chem Chem Phys* 2001, 3, 4722–4732.
49. Bonard, A.; Daele, V.; Delfau, J. L.; Vovelle, C. *J Phys Chem A* 2002, 106, 4384–4389.
50. Mulenko, S. A. *Rev Roum Phys* 1987, 32, 173–178.
51. Smith, G. P.; Golden, D. M.; Frenklach, M.; Moriarty, N. W.; Eiteneer, B.; Goldenberg, M.; Bowman, C. T.; Hanson, R. K.; Song, S.; Gardiner, Jr., W. C.; Lissianski, V. V.; Qin, Z. Available at [http://www.me.berkeley.edu/gri\\_mech/](http://www.me.berkeley.edu/gri_mech/), 1999.
52. Liu, I.; Cant, N. W.; Bromly, J. H.; Barnes, F. J.; Nelso, P. H.; Haynes, B.F. *Chemosphere* 2001, 42, 583–589.
53. Sehested, J.; Sehested, K.; Platz, J.; Egsgaard, H.; Nielsen, O. J. *Int J Chem Kinet* 1997, 29, 627–636.
54. Loucks, L. F.; Laidler, K. J. *Can J Chem* 1967, 45, 2767–2773.
55. Li, Q. S.; Zhang, Y.; Zhang, S. *J Phys Chem A* 2004, 108, 2014–2019.
56. Sahetchian, K. A.; Rigny, R.; De Maleissye, J. T.; Batt, L.; Anwar-Khan, M.; Matthews, S. *Proc Combust Inst* 1992, 24, 637–643.
57. Curran, H. J.; Pitz, W. J.; Westbrook, C. K.; Dagut, P.; Boettner, J.-C.; Cathonnet, M. *Int J Chem Kinet* 1998, 30, 229–241.
58. Walker, R. W. *Proc Combust Inst* 1988, 22, 883–892.
59. Alzueta, M. U.; Muro, J.; Bilbao, R.; Glarborg, P. *Israel J Chem* 1999, 39, 73–86.
60. Li, J.; Kazakov, A.; Dryer, F. L. *Int J Chem Kinet* 2001, 33, 859–867.
61. Bowman, C. T.; Golden, D. M.; Hanson, R. K.; Pitsch, H.; Davidson, D. F.; Bardos, A.; Cook, R.; Hong, Z.; Iyengar, P.; Shashank, S.; Vasu, S.; Walters, K.; Malhotra, R. GCEP Technical Report 2006; available at <http://gcep.stanford.edu/pdfs/QeJ5maLQQuGiSYMF3ATDA/2.6.5.bowman.06.pdf>.
62. Ruscic, B.; Wagner, A. F.; Harding, L. B.; Asher, R. L.; Feller, D.; Dixon, D. A.; Peterson, K. A.; Song, Y.; Qian, X. M.; Ng, C. Y.; Liu, J. B.; Chen, W. W. *J Phys Chem A* 2002, 106, 2727–2747.
63. Herbon, J. T.; Hanson, R. K.; Golden, D. M.; Bowman, C. T. *Proc Combust Inst* 2002, 29, 1201–1209.
64. Kee, R. J.; Rupley, F. M.; Miller, J. A. Technical Report SAND89-8009, Sandia National Laboratories, Albuquerque, NM, 1989.
65. Cool, T. A.; Wang, J.; Hansen, N.; Westmoreland, P. R.; Dryer, F. L.; Zhao, Z.; Kazakov, A.; Kasper, T.; Kohse-Höinghaus, K. *Proc Combust Inst* 2007, 31, 285–294.
66. Kee, R. J.; Grcar, J. F.; Smooke, M. D.; Miller, J. A., Technical Report SAND85-8240, Sandia National Laboratories, Albuquerque, NM, 1985.
67. Kee, R. J.; Dixon-Lewis, G.; Warnatz, J.; Coltrin, M. E.; Miller, J. A. Technical Report SAND86-8246, Sandia National Laboratories, Albuquerque, NM, 1986.
68. Zhao, Z.; Kazakov, A.; Dryer, F.L. *Combust Flame* 2004, 139, 52–60.
69. Law, C. K.; Jomaas, G. Personal communication, 2004.
70. Egolfopoulos, F. N.; Law, C. K. *Combust. Flame* 1990, 80, 7–16.
71. Chen, Z.; Qin, X.; Ju, Y.; Zhao, Z.; Chaos, M.; Dryer, F. L. *Proc Combust Inst* 2007, 31, 1215–1222.